LAWRENCE
LIVERMORE
NATIONAL
LABORATORY

Carbon deposition during brittle rock deformation: Changes in electrical properties of fault zones and potential geoelectric phenomena during earthquakes

E. A. Mathez, J. J. Roberts, A. G. Duba, A. K. Kronenberg, S. L. Karner

May 16, 2008

Disclaimer

This document was prepared as an account of work sponsored by an agency of the United States government. Neither the United States government nor Lawrence Livermore National Security, LLC, nor any of their employees makes any warranty, expressed or implied, or assumes any legal liability or responsibility for the accuracy, completeness, or usefulness of any information, apparatus, product, or process disclosed, or represents that its use would not infringe privately owned rights. Reference herein to any specific commercial product, process, or service by trade name, trademark, manufacturer, or otherwise does not necessarily constitute or imply its endorsement, recommendation, or favoring by the United States government or Lawrence Livermore National Security, LLC. The views and opinions of authors expressed herein do not necessarily state or reflect those of the United States government or Lawrence Livermore National Security, LLC, and shall not be used for advertising or product endorsement purposes.

1

2

Carbon deposition during brittle rock deformation: Changes in electrical

properties of fault zones and potential geoelectric phenomena during earthquakes

5

E.A. Mathez[1], J.J. Roberts[2], A.G. Duba[1], A.K. Kronenberg[3], and S.L. Karner[4]

7

[1]Department of Earth and Planetary Sciences, American Museum of Natural History,

New York, NY, 10024, mathez@amnh.org, duba@amnh.org

[2]Lawrence Livermore National Laboratory, POB 808, L-201, Livermore, CA 94550,

roberts17@llnl.gov

[3]Center for Tectonophysics, Department of Geology and Geophysics, Texas A&M

University, College Station, TX, 77843, kronenberg@geo.tamu.edu

[4]ExxonMobil Upstream Research Co., POB 2189, Houston, TX 77252,

stephen.l.karner@exxonmobil.com

16

16 **Abstract**

17 To investigate potential mechanisms for geoelectric phenomena accompanying

18 earthquakes, we have deformed hollow cylinders of Sioux quartzite to failure in the

19 presence of carbonaceous pore fluids and investigated the resulting changes in electrical

20 conductivity and carbon distribution. Samples were loaded at room temperature or $400^{o}C$

21 by a hydrostatic pressure at their outer diameter, increasing pressure at a constant rate to

22 ~290 MPa. Pore fluids consisted of pure CO, CO_2, CH_4 and a 1:1 mixture of CO_2 and

23 CH_4, each with pore pressures of 2.0 to 4.1 MPa. Failure occurred by the formation of

24 mode II shear fractures transecting the hollow cylinder walls. Radial resistivities of the

25 cylinders fell to 2.9 to 3.1 MΩ-m for CO tests and 15.2 to 16.5 MΩ-m for CO_2:CH_4 tests,

26 compared with >23 MΩ-m for dry, undeformed cylinders. Carbonaceous fluids had no

27 discernable influence on rock strength. Based on mapping using electron microprobe

28 techniques, carbon occurs preferentially as quasi-continuous films on newly-formed

29 fracture surfaces, but these films are absent from pre-existing surfaces in those same

30 experiments. The observations support the hypothesis that electrical conductivity of

31 rocks is enhanced by the deposition of carbon on fracture surfaces and imply that

32 electrical properties may change in direct response to brittle deformation. They also

33 suggest that the carbon films formed nearly instantaneously as the cracks formed.

34 Carbon film deposition may accompany the development of microfracture arrays prior to

35 and during fault rupture and thus may be capable of explaining precursory and coseismic

36 geoelectric phenomena.

37 **1. Introduction**

38   Despite the sophistication of mechanical models of stable and unstable slip on

39   faults, earthquake rupture is controlled by rules that we have yet to discover, with

40   occurrences that confound our attempts at prediction. At the same time, a number of

41   anomalies have been reported, such as transient electrical phenomena, which are most

42   obvious as coseismic signals and have sometimes been reported as precursory anomalies

43   prior earthquake events.

44   There has been considerable effort in laboratory programs to investigate rock

45   deformation as applied to brittle failure and seismogenesis. For example, studies have

46   been conducted on stability analysis of brittle failure [e.g., *Brace and Byerlee,* 1966;

47   *Lockner et al.,* 1986; *Marone and Scholz,* 1988; *Blanpied et al.,* 1991], on dynamic

48   properties of failure and frictional sliding [e.g., *Johnson and Scholz,* 1976; *Dieterich,*

49   1986; *Roy and Marone,* 1996], on strength recovery during the seismic cycle [e.g.,

50   *Frederich and Evans,* 1992; *Karner et al.,* 1997; *Karner and Marone,* 2000; *Beeler et al.,*

51   2001], and on the chemo-mechanical properties of fluid-rock interactions [e.g., *Chester*

52   *and Higgs,* 1992; *Karner and Schreiber,* 1993; *Dewers and Hajash,* 1995; *Scholz et al.,*

53   1995; *Olsen et al.,* 1998]. Nonetheless, the question of what happens in the Earth

54   endures in part because laboratory experiments have not completely addressed the natural

55   phenomena.

56   Fluids are commonly implicated as being involved in seismogenesis and transient

57   electrical phenomena. For example, fault-zone studies indicate that fluid-rock

58   interactions alter rock strength and fault zone properties [e.g., *Cao and Aki,* 1986;

59   *Kobayashi et al.,* 2001; *Tadokoro and Ando,* 2001; *Uda et al.,* 2001], and geologic

60   observations near active fault zones suggest a complex interplay between seismogenesis

61   and fluid-rock interactions on the one hand and various physical phenomena on the other.

62   The latter include geo-electrical [e.g., *Madden et al.,* 1993; *Chu et al.,* 1996; *Murakami et*

63   *al.,* 2001; *Yang et al.,* 2002], electrical discharge [e.g., *Enomoto and Zheng,* 1998] and

64   magneto-telluric signals [e.g., *Fraser-Smith et al.,* 1990; *Sumitimo et al.,* 1997; *Park et*

65   *al.,* 2007a]. How these processes are related remains unclear.

66   Also unclear is exactly how fluids influence electrical properties of rocks.

67   Interstitial brines could determine those properties (e.g., see review of *Jones* [1992]) and

68   by inference, electrical properties around highly porous, fractured fault zones. Evidence

69   exists, however, that electrical properties may more commonly be governed by the

70   formation of graphitic or other carbonaceous precipitates on the fracture surfaces rather

71   than by brines within the fractures. For example, there are well-documented cases in

72   which deformation of rocks has occurred by brittle microcracking in the presence of

73   carbonaceous fluids [*Selverstone*, 2005], and fracture networks coincident with

74   microscopic to mesoscopic graphitic deposits are not uncommon in many rocks [e.g.,

75   *Frost et al.,* 1989; *Mareschal et al.,* 1992; *Mathez et al.,* 1995; *Gray et al.,* 1998; *Mogk*

76   *and Mathez,* 2000]. More generally, laboratory electrical resistivity measurements and

77   observations of carbon on fracture surfaces suggest that the electrical conductivity of the

78   crust may commonly be governed by carbon in the microfracture network [e.g.,

79   *Shankland et al.,* 1997], not by interstitial brines as often supposed.

80   Of relevance to the possible role of fluids in geo-electrical signals and

81   disturbances of the electromagnetic spectrum associated with earthquakes are the

82   experiments of *Roberts et al.* [1999]. They observed that slight increases in electrical

83   conductivity occurred concomitant with the formation of microfractures in samples

84 deformed in the presence of CO_2-CO and CO_2-CH_4 fluids. They interpreted the results to

85 indicate that electrical conductivity increased due to the instantaneous deposition of

86 carbon on the newly-formed crack surfaces. They then speculated that if this

87 phenomenon occurs as rocks dilate prior to earthquake rupture along a fault, it could

88 account for some of the observed disturbances in the electromagnetic field associated

89 with seismogenesis.

90   The *Roberts et al.* [1999] experiments were complex and their conclusions

91 correspondingly uncertain. Accordingly, we have conducted a series of simpler

92 experiments designed (1) to test one of their key conclusions that carbonaceous films

93 form rapidly on newly-formed microfracture surfaces in the presence of a carbonaceous

94 atmosphere, (2) to confirm that deposition of carbonaceous films results in an increase in

95 electrical conductivity of the bulk rock by forming an interconnected circuit on a

96 microfracture network, and (3) to determine if carbonaceous fluids affect rock strength.

97 The new experiments demonstrate that carbon films instantaneously form on new fracture

98 surfaces with a consequent increase in electrical conductivity, but that carbonaceous

99 fluids do not appear to have a measurable influence on rock strength.

100 **2. Original experiments**

101   The *Roberts et al.* [1999] experiments involved applying a uniaxial load to

102 unjacketed cylinders of Nugget sandstone, St. Peter sandstone, and Westerly granite

103 while simultaneously monitoring changes in electrical resistance within the sample. The

104 rock cylinders were placed in an internally-heated gas-pressure vessel, heated to

105 temperatures of 350 to 500°C and exposed to fluids consisting of 5% CO + 95% CO_2, 5%

106 CH_4 + 95% CO_2, and 100% Ar, at pressures of 130 to 140 MPa. The apparatus produced

107 strain rates between 10^{-6} and 10^{-5} s^{-1}, so the samples experienced an extended period of

108 dilation before catastrophically failing.

109   Results of a typical experiment are shown in Figure 1. The motor of the loading

110 system was driven at its maximum rate until load was observed to increase sharply (at 1.5

111 hr). The rate was then decreased to achieve a sample strain rate of ~10^{-6} s^{-1}. As load

112 steadily increased, so did resistance until ~2.5 hr, after which it leveled off. The steady

113 increase in resistance may have been caused by the sample drying out, by a change in

114 oxidation state, or by a progressive destruction of current-bearing pathways. Despite

115 these complexities, the experiments revealed two interesting phenomena. The load twice

116 displayed small decreases that were accompanied by small decreases in resistance, and

117 immediately preceding catastrophic failure resistance exhibited a precipitous drop from

118 ~150 to 100 MΩ. Subsequent study of the samples suggested the presence of carbon in

119 conjugate sets of microfractures produced during dilatant sample failure.

120   These observations form the basis of the hypothesis stated above that it was the

121 instantaneous deposition of carbon on the newly-formed fracture surfaces that caused

122 resistance to drop when fractures form. Indeed, the interpretation is consistent with the

123 expectation that any new surface should instantaneously react with whatever mobile

124 phase is present to produce an adsorbed layer several monolayers or more thick.

125   A major problem of the earlier experiments was that the failed cylinders were not

126 amenable to analytical studies. The post-run products were friable cones from near the

127 ends of the original cylinders, and it was difficult to distinguish between surfaces that

128 existed prior to the experiment of the porous samples, and conjugate fracture surfaces

129 formed during deformation.

130   **3. Experimental design and procedure**

131   **3.1. Deformation**

132   The current deformation experiments were done in the John Handin Rock

133   Deformation Laboratory at Texas A & M University using a triaxial Heard-type gas

134   apparatus with hardened Inconel 725 pistons designed to allow access of reactive pore

135   fluids and measurement of temperature at one end of the sample. Temperature, confining

136   pressure and pore pressure conditions were chosen to ensure that deformation involved

137   brittle fracture at all scales of observation. Temperatures were measured using a

138   chromel-alumel thermocouple and pressures were measured using strain-gauge-type

139   transducers (a BLH transducer was used for the elevated confining pressure

140   measurements while a high-sensitivity Honeywell transducer was used for the relatively

141   low pore pressure measurements). The deformed samples were stored in dry N_2 and

142   delivered to either the American Museum of Natural History for carbon mapping and

143   SEM examination or to Lawrence Livermore National Laboratory for electrical resistivity

144   measurements.

145   A major goal of the current experiments was to recover intact charges for the

146   analytical investigations. In order to achieve this, deformation experiments were

147   performed on hollow cylinders of Sioux quartzite (Figure 2) by increasing the confining

148   pressure applied to the outer diameter of silver-jacketed samples while holding an

149   internal pore pressure constant. Sioux quartzite was chosen for its purity, its simple,

150   recrystallized texture and its low-porosity (<1%). The mechanical characteristics of

151   Sioux quartzite are known from previous deformation studies [*Krech et al*., 1974; *Peck*

152   *and Gordon*, 1982; *Mardon et al*., 1990]. The hollow cylinder configuration was adopted

153   to reach the high differential stresses needed for failure of dense, crystalline quartzite and

154   to maximize access of the internal fluid to the specimen pore space, while minimizing the

155   dimensions across which electrical resistance was to be measured. The hollow cylinders

156   dimensions were ~20 mm in length, 8.86 ($\pm$0.02) mm in diameter, and 1.22 ($\pm$0.05) mm

157   in wall thickness. In addition, to prevent catastrophic failure and collapse, the cylinders

158   were filled with clean, loose quartz sand (20/40 mesh, US Silica). The sand served two

159   additional purposes. First, the large volume of pore space of the sand provided a large

160   reservoir for the carbonaceous fluid. Second, the surfaces of the quartz sand grains,

161   which were in contact with the carbonaceous fluid for the duration of each experiment,

162   offered a control against which carbon films on the newly formed surfaces in the

163   quartzite cylinder could be compared. As expected, deformation produced several

164   distinct sets of easily-recognized, through-going fractures, but the cylinders remained

165   intact in their jackets to the extent that radial resistance could be measured and samples

166   could be cut and polished without epoxy injection for SEM observation and electron

167   probe measurement.

168   Most of the deformation experiments were performed at a temperature of 400

169   ($\pm$1)°C for durations (from the time that 400°C was reached) of up to ~9.8 x 10^4 s, and

170   one experiment was performed at room temperature (25°C). Maximum confining

171   pressures ranged from 178 to 290 ($\pm$3) MPa, while pore fluid pressures (introduced at the

172   inner, unjacketed wall) were maintained constant during each experiment at values of 0 to

173   4.23 ($\pm$0.01) MPa.

174   The quartzite samples were jacketed by annealed silver tubing (mechanically

175   sealed at the pistons) and hydrostatically loaded at room temperature using Ar gas as the

176 confining fluid applied to the outer wall of samples to an initial pressure of ~100 MPa.

177 Silver jackets were leak-tested before raising temperature to 400°C and introducing the

178 pore fluid. Time t was monitored in all experiments, setting $t = 0$ at the moment that the

179 experimental temperature was reached. Confining pressure in each experiment was

180 increased at a constant rate (~0.09 - 0.20 MPa/s), either until the cylinder failed or until a

181 pre-determined, subcritical stress was achieved. The latter was chosen as a fraction of the

182 mean, short-term failure strength. The value of time at maximum confining pressure for

183 each sample (Table 1) corresponds to the time that the confining pressure reached 90% of

184 the ultimate failure pressure (for samples that were loaded to failure). For samples that

185 were loaded to a constant, subcritical confining pressure, the value of time at maximum

186 confining pressure corresponds to the time that the maximum subcritical pressure was

187 applied.

188 Quartzite is brittle under the experimental conditions, and the silver jackets tended

189 to rupture when samples reached their failure strength, allowing Ar gas to leak into the

190 sample through the torn jacket. Upon failure, temperature was reduced to 100°C within

191 60 s to prevent loss of carbon from fracture surfaces. Confining pressure-time plots

192 (Figure 3) illustrate the application of pressure and, in cases that samples failed, the

193 sudden drop in pressure due to the rapid loss of Ar through the ruptured silver jacket.

194 Piezoelectric transducers were used to detect acoustic emissions associated with

195 microcracking, but increased rates of emissions above electronic background levels were

196 difficult to detect prior to sample failure. Acoustic emissions above background levels

197 were largely restricted to the time that samples failed.

198 Elastic stress states in the hollow cylindrical samples prior to failure are given by

9

199

$$\sigma_\theta = \frac{P_e \left(\frac{b}{a}\right)^2 \left[1+\left(\frac{a}{r}\right)^2\right]}{\left(\frac{b}{a}\right)^2 - 1}$$ [1]

202

203

$$\sigma_r = \frac{P_e \left(\frac{b}{a}\right)^2 \left[1-\left(\frac{a}{r}\right)^2\right]}{\left(\frac{b}{a}\right)^2 - 1}$$ [2]

206

207

208

$$\sigma_z = P_e$$ [3]

210

211   where the effective pressure P_e is given by the difference between confining and pore

212   pressures, r is the radial position in the sample, and a and b are the inner and outer wall

213   radii, respectively [*Timoshenko and Goodier*, 1970]. Maximum differential stresses (σ_θ -

214   σ_r) are obtained at the inner wall, where the effective σ_r is zero and the stress state is

215   biaxial.

216   No corrections to reported stresses were made for the strength of the silver jacket,

217   given that (1) annealed silver has low flow strengths at T = 400°C, (2) only small elastic

218   distortions of the silver jacket were required as samples were loaded radially by

219   application of confining pressure, and (3) initiation of sample failure is expected at the

220   unjacketed inner wall of the sample. We also did not make corrections to account for any

221   loads supported by the quartz sand placed within the hollow quartzite cylinders. While

222   we attempted to place as much sand within this space as possible, the sand was not

223   ideally close-packed, and Hertzian contact loads are expected to have been

224   correspondingly small. Any thermal expansion of the quartz sand during heating must

225   have been similar to that of the quartzite cylinder.

226   **3.2. Pore fluids**

227   The Sioux quartzite cylinders were deformed with pore fluids consisting of CO,

228   CO_2, CH_4, a 1:1 mixture of $CO_2 + CH_4$, and air. Under the run conditions, condensed

229   carbonaceous phases are unstable in the presence of air or of pure CO_2 and CH_4, so any

230   carbon produced in the presence of these gases must have formed by non-equilibrium

231   processes, such as adsorption on newly-formed surfaces. In contrast, the CO and $CO_2 +$

232   CH_4 fluids are metastable and should spontaneously react to form graphite (Figure 4) via

233   the well-known Boudard reaction,

234   $$2CO \rightarrow C + CO_2, \qquad\qquad [4]$$

235   or by

236   $$CO_2 + CH_4 \rightarrow 2C + 2H_2O. \qquad\qquad [5]$$

237   Despite the metastability of the CO and $CO_2 + CH_4$ fluids, graphite was never observed

238   as a recognizable, macroscopic phase in any of the run products. On the other hand, new

239   surfaces clearly display distinct carbonaceous films. No attempt was made to

240   characterize film compositions. In addition, rarely one encounters distinct regions of

241   relatively high carbon concentrations ($\approx$ 10 - 20%) in the cracks. Whether or not these

242   are individual grains, particularly thick coatings, or[jjr1] contamination from the

243   polishing procedure is not known[jjr2].

244   Graphite is stable under the conditions of oxygen fugacity (fO_2) that prevail

245   throughout much of the crust [e.g., *Holloway,* 1984; *Jodicke,* 1992]. Except under very

246   low pressure, the fluid in equilibrium with graphite consists of nearly pure CO_2 and very

247   little CO (Figure 4). This simply points to the fact that graphite formation proceeds

248   through an intermediate step,

249                              $$CO_2 \rightarrow CO + 1/2O_2$$ [6]

250   and that reaction [4] describes its precipitation for all CO_2:CO ratios. In other words,

251   even though CO-rich gases are extremely rare in nature, the Boudard reaction is an

252   accurate mechanistic representation of carbon formation for all $CO + CO_2$ gases. The

253   logic of the present experimental design is in part based on this fact.

254   **3.3. Electrical conductivity measurements**

255   Resistivity of deformed samples was measured radially across the wall thickness

256   of hollow cylinders. To prepare for resistivity measurements the quartz sand was

257   removed from the cylinders and preserved. The outer silver jacket was used as one

258   electrode and a thin gold foil in contact with the inner wall was used as another electrode.

259   Electrical contact of the outer silver jacket was insured by the application of confining

260   pressure during the experiment prior to electrical properties measurements. Electrical

261   contact of the inner gold foil was accomplished by inflating a bladder (using a gas

262   pressure of 0.3 - 0.4 MPa) within the sample to press the gold foil tightly against the

263   inner surface.

264   Electrical resistivity was measured with a HP 4284A LCR meter at 1 kHz

265   frequency and 1 V signal amplitude. The highest resistance measurable by this system is

266   100 MΩ. To convert from resistance to resistivity or conductivity the sample geometry

267 must be taken into account. Post-experiment electrical measurements were only

268 performed on samples that maintained a relatively uniform cylindrical geometry. The

269 length, ID, and OD were each measured in five places and the average used to calculate

270 the effective geometric factor according to

271 $$GF = 2\pi length/[\ln(OD/ID)],\qquad\qquad[7]$$

272 which is valid for a hollow cylinder. The geometric factors ranged from 0.15 to 0.30

273 meters, depending primarily on the individual sample length.

274 Taking into account the geometry of the samples and the instrument impedance

275 limit, the maximum measurable resistivity is 23 MΩ-m (corresponding to a minimum

276 conductivity of 4.4 x 10^{-8} S/m).

277 **3.4. SEM and carbon mapping**

278 For SEM imaging and carbon analysis, the Sioux quartzite cylinders were cut

279 perpendicular to their axes with a thin-kerf diamond saw in slices about 0.5 cm thick.

280 The slices were glued to glass slides with epoxy and the exposed surfaces polished in

281 alumina/water slurries down to 0.3 μm grit size. Care was taken to avoid exposing the

282 surfaces to be polished to the epoxy. However, it was discovered that despite the 0.5 cm

283 sample heights, the epoxy wicked up through the fractures of a few samples to

284 contaminate that surface. Samples contaminated in this way were not used for any of the

285 analytical results. Samples prepared subsequent to discovery of the problem were

286 mounted in high-viscosity, fast-drying epoxy, which did not wick into the sample or

287 affect carbon analyses. Carbon maps were also made for surfaces of the quartz sand that

288 filled the cylinders. The sand was analyzed by pressing several dozen grains from each

13

289   experiment into In metal and then mapping carbon distribution on several, relatively flat

290   sand grain surfaces.

291   As illustrated below, the polished surfaces intersect sets of fractures formed

292   during deformation, so that the surfaces of the fractures are exposed at the intersections.

293   Standard electron probe maps of carbon distribution were produced using the Cameca

294   SX100 instrument at the American Museum of Natural History. Analytical conditions

295   were 10 kV acceleration potential and 40 nA beam current. The particular set of

296   operating conditions together with the use of a large, Ni-C multilayer (LPC2) diffracting

297   crystal yielded a count rate of ~ 76,000 c/s on graphite. The spot-densities of the maps

298   were normalized to a common value based on the count rate obtained on a graphite

299   standard. Prior to analysis, the samples were coated with ~10 nm of either Ag or Au-Pd.

300   Ag coats are somewhat more transparent to carbon x-rays compared to Au-Pd coats of

301   similar thickness, and they were also found to absorb much less carbon from the ambient

302   atmospheres to which they were exposed. However, Ag coats oxidize with time with

303   consequent degradation of surface conductivity, while Au-Pd coats remain inert.

304   Practically, this meant that samples coated with Ag had to be inserted into the probe and

305   analyzed immediately, and it was generally not possible to image them later with

306   secondary electrons in the SEM. Therefore, most samples were coated with Au-Pd.

307   **4. Results**

308   **4.1. Mechanical properties**

309   The mechanical results of the compression experiments are listed in Table 1. The

310   principal effective stresses σ_Θ, σ_r, and σ_z in all samples were determined using the elastic

311   solution (eqns 1-3) of *Timoshenko and Goodier* [1970] for a cylindrical body loaded by

312 an effective pressure P_e (= confining pressure P_c – pore pressure P_p) at its outer diameter.

313 As illustrated for sample Q6 at its peak P_e (at P_c = 245.5 MPa, P_p = 4.14 MPa) just prior

314 to failure (Figure 5), the value of σ_Θ is greatest at the inner diameter ($r = a$), σ_r is zero at

315 the unjacketed inner wall ($r = a$) and rises to P_e at the outer diameter ($r = b$), and σ_z is

316 constant (= P_e) throughout the sample. Thus, differential stress (σ_Θ - σ_r) is maximum

317 (Figure 6) at the sample's inner wall (=1095 MPa at failure, and considerably larger than

318 P_e) where effective stress is biaxial ($\sigma_\theta > \sigma_z > \sigma_r = 0$). Differential stresses determined as

319 a function of time are valid as P_c (and P_e) rises with time prior to failure (Figure 3), but

320 stress states are poorly known when P_c (and P_e) drops after failure. Once brittle

321 deformation begins, failure of the cylindrical sample is rapid; P_c and, presumably,

322 stresses σ_Θ, σ_r, and σ_z decrease quickly.

323   Compressive strengths, as determined by maximum differential stresses

324 calculated at failure of individual Sioux quartzite samples (Table 1) are relatively

325 uniform, with less scatter than is typically observed for brittle failure in conventional

326 triaxial compression experiments. Short-term compressive strengths (σ_θ - σ_r = 1110 ± 83

327 MPa, taking the mean of Q2, Q3, Q5, Q10, Q11, and Q12 for loading times $t < 250$s) are

328 large (Figure 7) given that one of the principal effective stresses (σ_r) is zero. The high

329 compressive strength is most likely associated with a low initial density of cracks and

330 interlocking nature of quartz grain boundaries. The high degree of reproducibility in

331 compressive strengths determined using the hollow cylinder geometry is attributed to 1)

332 the well-known stress state along most of the specimen's length, which is affected only

333 slightly by shear stresses at specimen contacts with the rigid pistons, 2) the uniformity of

15

334   the quartzite, and 3) the lack of a significant load contribution by the jacket at the outer

335   specimen diameter to fracture initiation at the inner specimen wall.

336   Compressive strength does not appear to be strongly affected by the carbonaceous

337   fluid present, with sample failure occurring at differential stresses (σ_θ- σ_r) of 1201 MPa

338   (Q3) in air, 1225 (Q2) and 1089 (Q5) MPa for the CO pore fluid, 1083 (10) and 1057

339   (Q11) MPa for the CO_2 pore fluid, and 1015 MPa (Q12) for the 50:50 CO_2/CH_4 pore

340   fluid. Compressive strength also does not appear to depend on the time of loading, with

341   failure of sample Q6 occurring at (σ_θ- σ_r) = 1095 MPa after loading for $t = 2.7$ x 10^3s.

342   Samples Q4 and Q9 did not fail despite loading at (σ_θ- σ_r) = 1037 and 1071 MPa,

343   respectively, for times of 2.5 x 10^4s and 1.4 x 10^4s. Thus, compressive strengths (> 1037

344   and > 1071 MPa) at these extended times appear to fall in the same range as the short-

345   term compressive strengths.

346   Comparing these results to earlier tensile strengths of Sioux quartzite ($\sigma_t \sim 11$

347   MPa) at room temperature and T = 412°C [*Mardon et al.*, 1990] yields a ratio of

348   compressive to tensile strength of 100:1 (Figure 7). This is much greater than 8:1

349   predicted by simple Griffith theory [*Jaeger and Cook*, 1976] or the ratio 14:1 observed

350   for porous quartz sandstone [*Bobich*, 2005].

351   **4.2. Development of fractures**

352   The hollow cylinders of Sioux quartzite failed by the development of macroscopic

353   shear (Mode II) fractures that parallel the specimen axis and transect the cylinder wall,

354   leading to the rupture of the silver jacket (Figure 8). Closer inspection of cut and

355   polished surfaces of the deformed cylinders reveals several additional populations of

356   microcracks that developed during heating and loading of samples and thus had differing

357   lifetimes while exposed to carbon-bearing pore fluids. These features are illustrated in

358   the SEM mosaics of Figure 9. Exposed at the surface are (1) rough microcracks at grain

359   boundaries; (2) smooth, concentric, intragranular cracks parallel to the cylinder walls; (3)

360   concentric, intragranular, *en echelon* cracks subparallel to the cylinder walls; (4)

361   macroscopic shear fractures that transect cylinder walls; and (5) open radial cracks the

362   distribution of which is related to macroscopic shear fractures.

363   The rough microcracks at grain boundaries lack preferred orientations relative to

364   the stress state during loading (Figure 2). Therefore, these microcracks are interpreted to

365   result from local stresses generated during heating associated with the large thermal

366   expansion anisotropy of quartz. Evidence for thermally-induced microcracking in Sioux

367   quartzite at P_c = 100 MPa was reported by *Mardon et al*., [1990] and implicated in a

368   reduction in tensile strength between 400 and 500°C. Since they formed first, the grain

369   boundary microcracks were exposed to the carbon-bearing pore fluid at the experimental

370   temperature for extended periods of time (i.e., t = 9.0 x 10^3s for Q6, see Table 1).

371   The concentric cracks parallel to cylinder walls are interpreted to be tensile (Mode

372   I) cracks that opened against the minimum principal stress (σ_r) in response to the stress

373   state generated by increasing P_c (Figure 2), whereas the concentric *en echelon* crack

374   arrays subparallel to cylinder walls are interpreted to be shear (Mode II) cracks. While

375   the opening of Mode I cracks likely preceded the development of Mode II cracks, the

376   lack of significant numbers of acoustic emissions prior to failure, in contrast to the

377   cascade of events that accompanied failure, suggests that the surfaces of both these types

378   of cracks were exposed to carbon-bearing pore fluid for very short times (< 10s for the

379   Mode I cracks and of the order of 1s for the Mode II cracks).

380   The failure of the hollow cylinders occurred by the development of macroscopic

381   shear (Mode II) fractures across the cylinder walls. This must have been followed

382   immediately by the collapse of the cylinder walls inward. We infer that the radial cracks

383   developed during this time. These cracks thus formed in tension in a new stress state

384   during failure that is not described by the stress solutions (eqns 1 - 3) for loading of an

385   intact hollow cylinder. The times during which the new surfaces of radial cracks were

386   exposed to the carbon-bearing pore fluid must also have been very short (of the order of

387   1s).

388   **4.3. Carbon on fracture surfaces**

389   The distribution of carbon in the experimental samples was mapped by electron

390   microprobe and some of those mapped regions imaged by SEM. In the maps, carbon

391   concentration is related to spot density. One such map along with its corresponding SEM

392   image is illustrated in Figure 10, where it can be seen that the carbon count rate

393   associated with the microcrack surfaces is greater than that from the polished surface.

394   The polished surfaces should be completely devoid of carbon, except for the fact that

395   carbon deposits as a consequence of cracking of pump oils from the ambient electron

396   probe atmosphere under beam loading. The polished surfaces thus provide a minimum

397   analytical "background."

398   Since the crack surfaces are coated by a thin film probably no more then tens of

399   nm thick, the electron beam likely passes completely through the layer. It is thus

400   conceivable that count rate is enhanced when the inclined crack surface is in certain

401   orientations relative to an identical surface normal to the incident electron beam because

402   the beam path through an inclined layer is longer than that through a layer normal to the

403 path. The two path lengths are related by $1/\cos\theta$; for example, the beam path length

404 through a layer inclined at 45° is 1.4 times that through a layer of similar thickness but

405 normal to the beam, so x-ray intensity could be greater by this proportion as well.

406 Despite such a dependence on surface orientation, the observed differences in carbon

407 concentration between polished and crack surfaces are substantially larger than calculated

408 for different orientations. Also, we were unable to find any systematic relation between

409 count rate and surface tilt.

410 A central question is why carbon formed on the crack surfaces. As noted, the CO

411 atmosphere is metastable with respect to graphite, so it is conceivable that graphitic films

412 simply deposited on all available surfaces as a consequence of the thermodynamic

413 driving force. To investigate this possibility, we examined the quartz sand, the surfaces

414 of which existed undisturbed and in direct contact with the pore fluid throughout the

415 deformation experiments. Numerous maps revealed no detectable carbon on the surfaces

416 of the quartz sand over and above that on the polished surfaces [cf., Figure 11a, b]. This

417 observation indicates that, despite the fact that graphite was thermodynamically stable

418 under run conditions, a solid carbon phase did not form on any of the pre-existing, free

419 surfaces.

420 It follows from the above discussion that the carbonaceous films on the

421 microcracks and fractures formed when those features formed, or essentially

422 instantaneously. This is supported by a second important observation, namely that the

423 carbon films are well-developed on all of the five different types of cracks described

424 above. As noted, these different cracks record the chronology of deformation, with the

425 radial cracks having formed last during collapse of the cylinder walls with catastrophic

19

426 failure and breach of the silver jackets. Furthermore, the carbon films are not obviously

427 thicker on the older, thermally-induced cracks. The observations suggest that films form

428 very quickly (within times of ~1 s), and once formed, do not rapidly increase in

429 thickness. We hypothesize that carbon films instantaneously and preferentially formed

430 on the cracks surfaces because the new surfaces catalyzed reaction [4].

431   In order to compare the amounts of carbon on the crack surfaces of different

432 samples, carbon counts per unit area (normalized to graphite) were measured for sample

433 areas on crack surfaces. The sample areas were chosen based on how clearly the crack

434 surfaces were defined in the images of carbon distribution, and their shape and extent

435 were manually defined in the image processing software. From these count densities, we

436 subtracted the count densities for areas on the adjacent polished surfaces. The clear result

437 from this analysis is that carbon preferentially exists on microcrack and fracture surfaces

438 (Figures 10 and 12). This observation holds for all of the experimental samples,

439 regardless of the composition of the pore fluid they were exposed to, although the

440 samples deformed in CO tend to have slightly more carbon than those deformed in other

441 fluids. Still, if real differences in the amounts or thicknesses of carbon films do indeed

442 exist from one sample to another, uncertainties in the measurement and analytical

443 methodologies are so large compared to the signal that it is not possible to

444 unambiguously distinguish those differences.

445 **4.4. Electrical Conductivity**

446   The radial electrical conductivity of dry, undeformed Sioux quartzite cylinders is

447 extremely small in the ambient laboratory atmosphere ($\leq 4 \times 10^{-8}$ S/m). Electrical

448 conductivity measurements were performed on six run products: Q0 (air), Q6, Q7, Q9

449   (CO) and Q12 and Q13 (CO_2:CH_4). The control sample Q0 showed no measurable

450   conductivity. The radial conductivity of Sioux quartzite cylinders that failed in pore

451   fluids that promote carbon deposition is measurably higher (2.2 to 4.6 x 10^{-7} S/m for CO

452   tests; ~ 6.5 x 10^{-8} S/m for CO_2:CH_4 tests), consistent with the observation that carbon is

453   present on the microcrack surfaces. The minimum enhancement in electrical

454   conductivity for samples with carbon-bearing microfractures over undeformed samples is

455   a factor of 2 (CO_2:CH_4) to 5 (CO).

456   **5.0 Discussion**

457   The present experiments support the interpretation of *Roberts et al.* [1999] that

458   increases in electrical conductivity may accompany fracture formation in the presence of

459   carbonaceous pore fluids due to the essentially instantaneous deposition of carbonaceous

460   material on fracture surfaces as they formed. The relatively small changes in resistivity

461   observed in the experiments depend on the complex and imperfect nature of the

462   conductive path defined by the network of cracks, which in turn is governed by crack

463   interactions as they nucleate and grow.

464   **5.1 Earthquake precursory electrical phenomena**

465   Although there is some controversy about the existence and causes of reported

466   precursory electrical phenomena prior to earthquakes [eg., *Fenoglio et al.*, 1995; *Merzer*

467   *and Klemperer*, 1997; *Murakami et al.*, 2001; *Yang et al.*, 2002; *Egbert*, 2002; *Thomas et*

468   *al.*, 2007; *Park et al.*, 2007a; *Fraser-Smith et al.*, 1990], the results of the present

469   experiments and those of *Roberts et al.* [1999] suggest that the deposition of

470   carbonaceous material on new surfaces during microcracking in dilating fault zones may

471   decrease resistivity prior to seismic rupture. Indeed, the time periods over which changes

472 in resistivity must occur are readily explained by the very short times required for carbon

473 film deposition in our experiments. That carbon films do not appear to thicken with time

474 following initial deposition suggests that resistivity of the fault zone will change only as

475 new cracks are formed, not during frictional sliding on populations of previously-formed

476 cracks.

477 One difficulty with this interpretation is that the changes in resistivity required by

478 the apparent precursory phenomena appear to be much larger than those measured in our

479 experiments [Egbert, 2002]. The resistivity decreases observed in the laboratory were

480 very small and only observable because sample resistivities were so high (in the $M\Omega$

481 range). Perhaps natural precursory phenomena brought about by carbon deposition on

482 the growing microcrack network may only be observable where resistivities around faults

483 are high.

484 In addition, some scaling of electrical resistivity changes in the laboratory and

485 nature may be required due to differences in crack densities in the experiments and fault

486 zones. The crack density in experimental sample Q6 (Figure 9), expressed as crack

487 surface area in a unit rock volume, is $\approx 7 \times 10^3 \text{ m}^{-1}$. Crack densities of plate-scale fault

488 zones, such as the Punchbowl fault of the San Andreas fault system, show systematic

489 variations from very high values of $4 \times 10^8 \text{ m}^{-1}$ in the central fault core [*Chester et al.*,

490 1993], where ultracataclasite marks the horizon of repeated rupture, to much lower values

491 in the surrounding damage zone and subsidiary faults, where crack densities decay with

492 distance to $\sim2 \times 10^4 \text{ m}^{-1}$ at > 100 m from the fault core. Assuming that carbon films may

493 be deposited on all crack surfaces in networks with much larger crack densities than in

494 our samples, correspondingly larger changes in electrical properties may be possible in

495 nature. Thus, resistivities may be low within the central regions of the damage zone, but

496 ultimately electrical properties of the rock at distance will reflect low crack densities

497 similar to those observed in our experimental samples.

498   Changes in electrical properties through a single earthquake cycle cannot be as

499 large as implied by the total fracture densities of the fault core, since the extant fractures

500 accumulate over many individual slip events. Based on seismological determinations of

501 energy release for individual earthquakes, new fracture surface areas generated during a

502 single event must be less than 10^{-2} of the total surface areas [*Chester et al.*, 2005]. Also,

503 changes in electrical properties during dilation may be difficult to detect because fault

504 core resistivities are likely to be relatively low to begin with.

505   Finally, faults with aqueous pore fluids may exhibit electrokinetic signals as fault

506 pore volumes change and pore fluid flow generates streaming potentials [*Morgan et al.*,

507 1989; *Pride*, 1994; *Reppert et al.*, 2001]. These processes will largely be precluded when

508 carbonaceous fluids occupy the pore space. Under these circumstances, transient currents

509 may be generated by sudden increases in fault core conductivity.

510 **5.2 Coseismic transient electrical phenomena**

511   Unlike precursory signals, coseismic transient electrical phenomena are well-

512 documented. In particular, *Park et al.* [2007a] reported changes in electrical potential of

513 ≈ 2.5 mV coincident with the 28 September 2004 M = 6.0 Parkfield earthquake. The

514 signal was recorded by a dipole array that straddled the fault in the immediate vicinity of

515 the rupture. No precursory phenomena distinguishable from the noise were observed.

516 *Park et al.* [2007a] interpreted the coseismic signal to have been generated by the flow of

517 groundwater toward the fault in the hours immediately following the main rupture.

518 However, we question whether groundwater flow can be so rapid as to account for the

519 observed changes in electrical potential.

520 Still, the origin of the coseismic signals remains unclear. The Parkfield event was

521 shallow (7.9 km), and the rocks in the region are relatively conductive. Maximum

522 resistivity within a km of the surface is 60 Ω-m and even at a depth of 9 km resistivity is

523 only hundreds of Ω-m [*Park et al.*, 2007b]. Under these circumstances subtle changes in

524 the resistivity structure that may accompany rock dilatancy prior to rupture would not be

525 observed because the changes would be much less than background resistivity. A more

526 likely place to observe such small changes in electrical potential signals may be in a

527 portion of the San Andreas fault at Carrizo Plain, where the regional rock resistivity is

528 much higher [*Park et al.,* 2007b].

529 **6.0 Conclusion**

530 The results of this study help to isolate the role of carbon deposition on fresh

531 fracture surfaces in altering the electrical properties of rocks. They indicate that carbon

532 deposition is limited on mature surfaces already covered by impurities, while carbon

533 deposition on freshly broken surfaces is extremely rapid. Taken together, the present

534 results and those of *Roberts et al.* [1999] indicate that electrical conductivity in rocks

535 may be enhanced due to carbon deposition on newly formed fracture surfaces. They also

536 demonstrate the possibility that changes in rock resistivities could occur during rock

537 dilatancy and failure due to deposition of carbonaceous material on new fracture surfaces.

538 The origin of coseismic electrical currents associated with the September 2004

539 Parkfield event remains mysterious. If carbon has indeed been deposited during dilation

540 and fracture during the many seismic events at Parkfield, the presence of carbon can be

541 tested by analyses of drill core obtained recently by the SAFOD (San Andreas Fault

542 Observatory at Depth) project. If carbon has been deposited on multiple generations of

543 microcracks within the fault cataclasites and ultracataclasites, the accumulation of carbon

544 during fault slip can readily be tested by probe analyses using methods described here. If

545 carbon accumulation is significant, we expect some contribution by carbon films on

546 microcracks to the high conductivity of the San Andreas fault zone observed by *Park et*

547 *al.* [2007b].

548

559

559   **References**

560   Beeler, N. M., S. H. Hickman, and T. -F. Wong (2001), Earthquake stress drop and

561   laboratory-inferred interseismic strength recovery, *J. Geophys. Res., 106*, 30701-

562   30713.

563   Blanpied, M. L., D. A. Lockner, and J. D. Byerlee (1991), Fault stability inferred from

564   granite sliding experiments at hydrothermal conditions, *Geophys. Res. Lett., 18*, 609-

565   612.

566   Bobich, J. K. (2005), Experimental analysis of the extension to shear fracture transition in

567   Berea sandstone, M.S. thesis, 52 pp., Texas A&M University, College Station, TX.

568   Brace, W. F. and J. D. Byerlee (1966), Stick-slip as a mechanism for earthquakes,

569   *Science, 153*, 990-992.

570   Cao, T. Q., and K. Aki (1986), Effect of slip rate on stress drop, *Pageoph., 124*, 515-529.

571   Chester, F. M., and N. G. Higgs (1992), Multimechanism friction constitutive model for

572   ultrafine quartz gouge at hypocentral conditions, *J. Geophys. Res., 97*, 1857-1870.

573   Chester, F. M., J. P. Evans, and R. L. Biegel (1993) Internal structure and weakening

574   mechanisms of the San-Andreas Fault, *J. Geophys. Res., 98*, 771-786.

575   Chester, J. S., F. M. Chester, and A. K. Kronenberg (2005) Fracture surface energy of the

576   Punchbowl fault, San Andreas system, *Nature, 437*, 133-136,

577   doi:10.1038/nature03942.

578   Chu, J. J., X. Gui, J. Dai, C. Marone, M. W. Spiegelman, L. Seeber, and J. G. Armbruster

579   (1996) Geoelectric signals in China and the earthquake generation process, *J.*

580   *Geophys. Res., 101*, 13869-13882.

26

581   Dewers, T., and A. Hajash (1995), Rate laws for water-assisted compaction and stress-

582   induced water-rock interaction in sandstones, *J. Geophys. Res.*, *100*, 13093-13112.

583   Dieterich, J. H. (1986), A model for the nucleation of earthquake slip, in: *Earthquake*

584   *Source Mechanics*, *AGU Geophys. Mono. Vol. 37*, edited by S. Das, J. Boatwright

585   and C.H. Scholz, pp. 227-236.

586   Egbert, G. D., (2002), On the generation of ULF magnetic variations by conductivity

587   fluctuations in a fault zone, *Pure and Applied Geophysics, 159*, 1205-1227.

588   Enomoto, Y., and Z. Zheng (1998), Possible evidence of earthquake lightning

589   accompanying the 1995 Kobe earthquake inferred from the Nojima fault gouge,

590   *Geophys. Res. Lett., 25*, 2721-2724.

591   Fenoglio, M. A., M. J. S. Johnston, and J. D. Byerlee (1995), Magnetic and electric fields

592   associated with changes in high pore pressure in fault zones: Application to the Loma

593   Prieta ULF emissions, *J. Geophys. Res., 100*, 12,951-12,958.

594   Fraser-Smith, A. C., A. Bernardi, P. R. McGill, M. E. Ladd, R. A. Helliwell, O. G.

595   Villard, Jr. (1990), Low-frequency magnetic field measurements near the epicenter of

596   the Ms 7.1 Loma Prieta earthquake, *Geophys. Res. Lett. 17,* 1465-1468.

597   Fredrich, J. T., and B. Evans (1992), Strength recovery along simulated faults by solution

598   transfer processes, in *Proc. 33rd Natl. Rock Mech. Symp.*, edited by W. Wawersik,

599   pp. 121-130, Balkema, Rotterdam.

600   Frost, B. R., W. S. Fyfe, K. Tazaki, and T. Chan (1989), Grain-boundary graphite in

601   rocks and implications for high electrical conductivity in the lower crust, *Nature, 340,*

602   134-136.

603   Gray, G. J., S. R. Lawrence, K. Kenyon, and C. Cornford (1998) Nature and origin of

604   "carbon" in the Archaean Witwatersrand Basin, South Africa, *J. Geol. Soc., London*,

605   *155*, 39-59.

606   Holloway, J. R. (1984), Graphite-CH_4-H_2O-CO_2 equilibria at low-grade metamorphic

607   conditions, *Geology, 12*, 455-458.

608   Jaeger, J. C., and N. G. W. Cook (1976), *Fundamentals of Rock Mechanics*, 2nd edition

609   pp. 277-282, Chapman and Hall, London.

610   Jodicke, H. (1992), Water and graphite in the earth's crust: An approach to interpretation

611   of conductivity models, *Sur. Geophys., 13*, 381-407.

612   Johnson, T. L., and C. H. Scholz (1976), Dynamic properties of stick-slip friction of

613   rocks, *J. Geophys. Res., 81*, 881-889.

614   Jones, A. G. (1992), Electrical properties of the continental lower crust, in *The Lower*

615   *Continental Crust,* edited by D. M. Fountain, R.J. Arculus and R.W. Kay, pp. 81-143,

616   Elsevier, New York.

617   Karner, S. L., and C. Marone (2000), Effects of Loading Rate and Normal Stress on

618   Stress Drop and Stick-slip Recurrence Interval, in *Geocomplexity and the physics of*

619   *earthquakes, AGU Mono. v. 120*, edited by J. B. Rundle, D. L. Turcotte, and W.

620   Klein, pp. 187-198.

621   Karner, S. L., C. Marone, and B. Evans (1997), Laboratory study of fault healing and

622   lithification in simulated fault gouge under hydrothermal conditions, *Tectonophysics*,

623   *277*, 41-55.

624 Karner, S. L., and B. C. Schreiber (1993), Experimental simulation of plagioclase

625   diagenesis at P-T conditions of 3.5 km burial depth, *Pure Appl. Geophys., 141*, 221-

626   247.

627 Kobayashi, K., S. Hirano, T. Arai, R. Ikeda, K. Omura, H. Sano, T. Sawaguchi, H.

628   Tanaka, T. Tomita, N. Tomida, T. Matsuda, and A. Yamazaki (2001), Distribution of

629   fault rocks in the fracture zone of the Nojima Fault at a depth of 1140 m:

630   Observations from the Hirabayashi NIED drill core, *Island-Arc, 10*, 411-421.

631 Krech, W. W., F. A. Henderson, and K. E. Hjelmstad (1974) A standard rock suite for

632   rapid excavation research, *U.S. Bureau Mines Report 7865*.

633 Lockner, D. A., R. Summers, and J. D. Byerlee (1986), Effects of sliding rate and

634   temperature on frictional strength of granite, *Pure Appl. Geophys., 124*, 445-469.

635 Mareschal, M., W. S. Fyfe, J. Percival, and T. Chan (1992), Grain-boundary graphite in

636   Kapuskasing gneisses and implications for lower-crustal conductivity, *Nature, 357,*

637   674-676.

638 Madden, T. R., G. A. LaTorraca, and S. K. Park (1993), Electrical conductivity variations

639   around the Palmdale section of the San Andreas Fault Zone, *J. Geophys. Res., 98*,

640   795-808.

641 Mardon, D., A. K. Kronenberg, J. Handin, M. Friedman, and J. E. Russell (1990),

642   Mechanisms of fracture propagation in experimentally extended Sioux quartzite,

643   *Tectonophysics, 182*, 259-278.

644 Marone, C. J. and C. H. Scholz (1988), The depth of seismic faulting and the upper

645   transition from stable to unstable slip regimes, *Geophys. Res. Lett., 15*, 621-624.

646 Mathez, E. A., A. G. Duba, C. L. Peach, A. Léger, T. J. Shankland, and G. Plafker

647 (1995), Electrical Conductivity and Carbon in Metamorphic Rocks of the Yukon-

648 Tanana Terrane, Alaska, *J. Geophys. Res., 100,* 10,187-10,196.

649 Merzer, M., and S. L. Klemperer (1997), On the generation of ULF magnetic variations

650 by conductivity fluctuations in a fault zone, *Pure and Applied Geophysics, 150*, 217-

651 248.

652 Mogk, D. W., and E. A. Mathez (2000), Carbonaceous films in mid-crustal rocks from

653 the KTB borehole, Germany, as characterized by time-of-flight secondary ion mass

654 spectrometry. *Geochemistry Geophysics Geosystems 1*, paper 2000GC000081**.**

655 Morgan, F. D., E. R. Williams, and T. R. Madden (1989) Streaming potential properties

656 of Westerly granite with applications, *J. Geophys. Res*., *94*, 12449-12461.

657 Murakami H., T. Hashimoto, N. Oshiman, S. Yamaguchi, Y. Honkura, N. Sumitomo

658 (2001), Electrokinetic phenomena associated with a water injection experiment at the

659 Nojima fault on Awaji Island, Japan, *The Island Arc, 10*, 244-251.

660 Olsen, M. P., C. H. Scholz, and A. Léger (1998), Healing and sealing of a simulated fault

661 gouge under hydrothermal conditions: Implications for fault healing, *J. Geophys.*

662 *Res., 103*, 7421-7430.

663 Park, S. K., W. Dalrymple, and J. C. Larsen (2007a), The 2004 Parkfield earthquake:

664 Test of the electromagnetic precursor hypothesis, *J. Geophys. Res., 112,* B5302,

665 doi:10.1029/2005JB004196.

666 Park, S. K., J. C. Larsen, and T.-C. Lee (2007b) Electrical resisitivity changes not

667 observed with the 28 September 2004 M6.0 Parkfield earthquake on the San andreas

668   fault, California. *J. Geophys. Res., 112,* B12305, doi:10.1029/2006JB004459.

669   Peck, L., and R. B. Gordon (1982) The effect of compressive stress on the fracture energy

670   of Sioux quartzite, *Geophys. Res. Letts*., *9*, 186-189.

671   Pride, S. (1994) Governing equations for the coupled electromagnetics and acoustics of

672   porous-media, *Phys. Rev. B*, *50*, 15678-15696.

673   Reppert, P. M., F. D. Morgan, D. P. Lesmes, and L. Jouniaux (2001) Frequency-

674   dependent streaming potentials, *J. Colloid and Interface Sci*., *234*, 194-203.

675   Roberts, J. J., A. G. Duba, E. A. Mathez, T. J. Shankland, and R. Kinzler (1999), Carbon-

676   enhanced electrical conductivity during fracture of rocks, *J. Geophys. Res., 104,* 737-

677   747.

678   Roy, M. and C. H. Marone (1996), Earthquake nucleation on model faults with rate- and

679   state-dependent friction: effects of inertia, *J. Geophys. Res., 101*, 13919-13932.

680   Scholz, C. H., A. Léger, and S. L. Karner (1995), Experimental diagenesis: Exploratory

681   results, *Geophys. Res. Lett., 22*, 719-722.

682   Selverstone, J. (2005) Preferential embrittlement of graphitic schists during extensional

683   unroofing in the Alps: the effect of fluid composition on rheology in low-

684   permeability rocks, *J. Metamorphic Geology*, *23*, 461-470.

685   Shankland, T. J., A. G. Duba, E. A. Mathez, and C. L. Peach (1997), Increase of

686   electrical conductivity with pressure as an indicator of conduction through a solid

687   phase in mid-crustal rocks, *J. Geophys. Res., 102,* 14,741-14,750.

688   Sumitimo, N., N. Oshiman, S. Sakanaka, T. Goto, H. Utada, Y. Sasai, M. Uyeshima, S.

689   Koyama, R. Ishikawa, Y. Honkura, H. Tsunakawa, S. Yamaguchi, H. Inokuchi, H.

690   Murakami, I. Shiozaki, Y. Tanaka, T. Hashimoto, T. Mogi, and T. Uchida (1997),

691   Tectonoelectric signal related with the occurrence of the 1995 Hyogo-ken Nanbu

692   earthquake (M 7.2) and preliminary results of electromagnetic observation around the

693   focal area, *Jour. Phys. Earth, 45*, 91-104.

694   Tadokoro, K., and M. Ando (2002), Evidence for rapid fault healing derived from

695   temporal changes in S wave splitting, *Geophys. Res. Lett., 29*, 6-1 to 6-4.

696   Thomas, J. N., J. J. Love, and M. J. S. Johnston (2007), Re-examining the reported

697   magnetic precursor to the 1989 Loma Prieta earthquake using magnetic field data

698   collected in the US and Japan during September and October 1989, *IUGG General*

699   *Assembly,* Abstract 4036, Perugia, Italy, July 2007.

700   Timoshenko, S. P., and J. N. Goodier (1970), *Theory of Elasticity*, 3rd edition, pp. 68-71,

701   McGraw-Hill Book Co., New York.

702   Uda, S. I., A. Lin, and K. Takemura (2001), Crack-filling clays and weathered cracks in

703   the DPRI 1800 m core near the Nojima Fault, Japan: Evidence for deep surface-water

704   circulation near an active fault, *Island-Arc, 10*, 439-446.

705   Yang, C. H., P. H. Cheng, J. I. You, and L. L. Tsai (2002), Significant resistivity changes

706   in the fault zone associated with the 1999 Chi-Chi earthquake, west-central Taiwan,
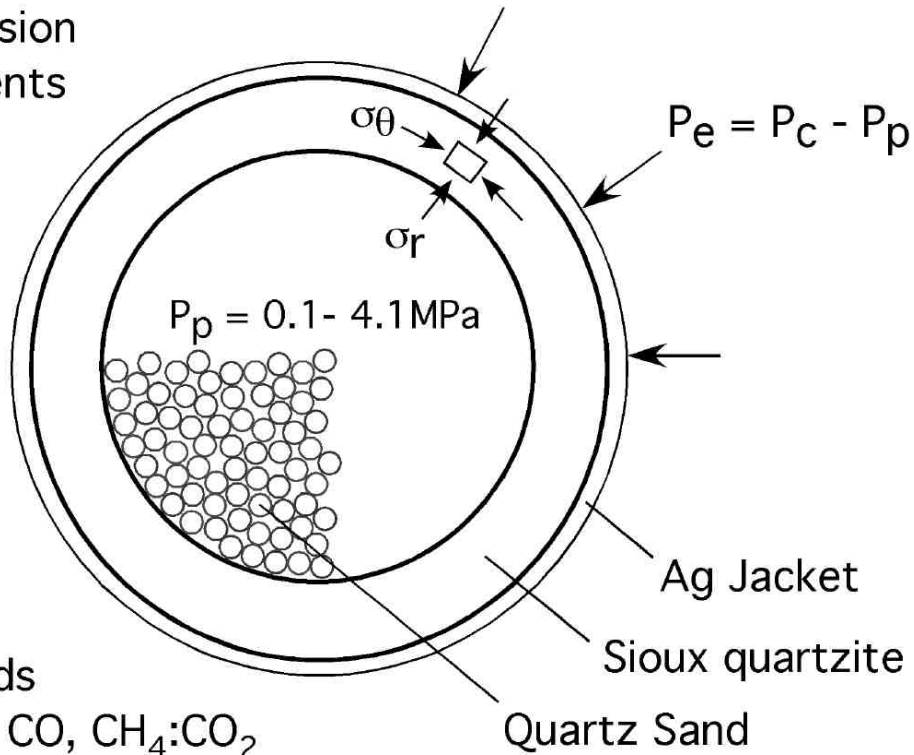
707   *Tectonophysics, 350*, 299-313.

708

708

709
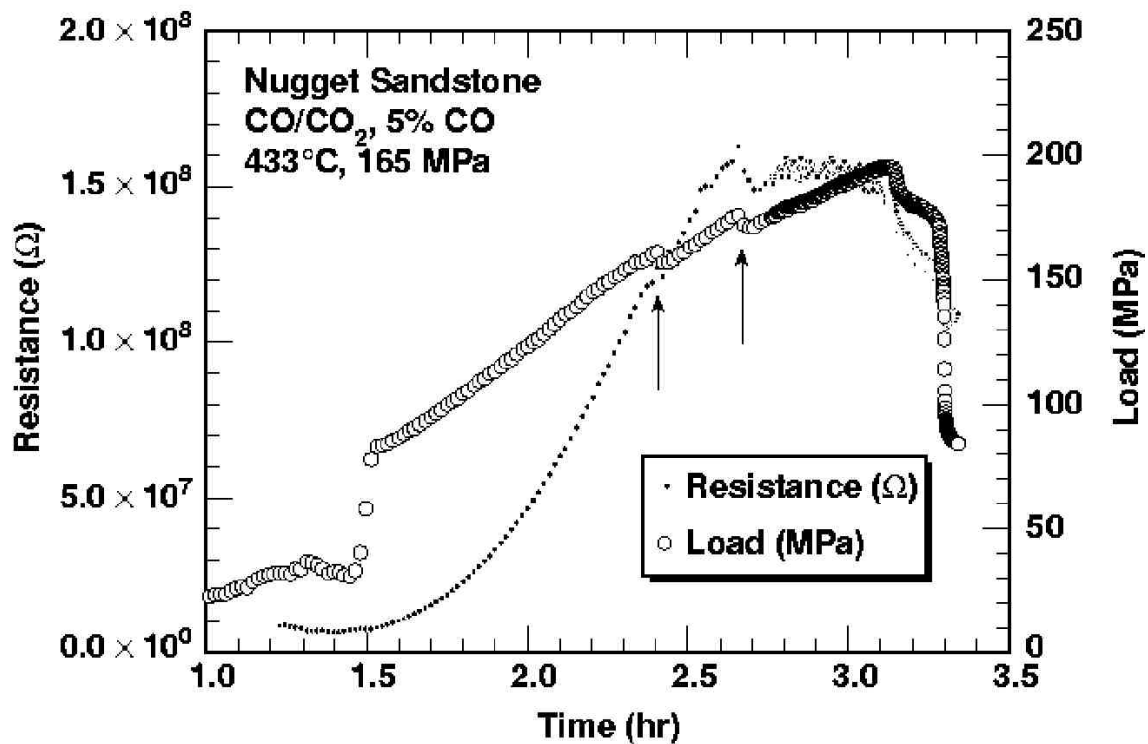
Figure 1. Electrical resistance (solid circles) and load (open circles) as a function of time

for Nugget sandstone. The unjacketed sample was deformed at 433°C in a CO-CO$_2$

atmosphere. After *Roberts et al.* [1999].

713

713

Figure 2. Hollow cylinders of Sioux quartzite were deformed to failure by increasing the

confining pressure P_c at the outer cylinder wall while maintaining a constant pore fluid

pressure P_p. Silver jackets were used to separate the sample from the argon confining

fluid while internal pore fluids were introduced at the unjacketed inner wall.

719

720

720
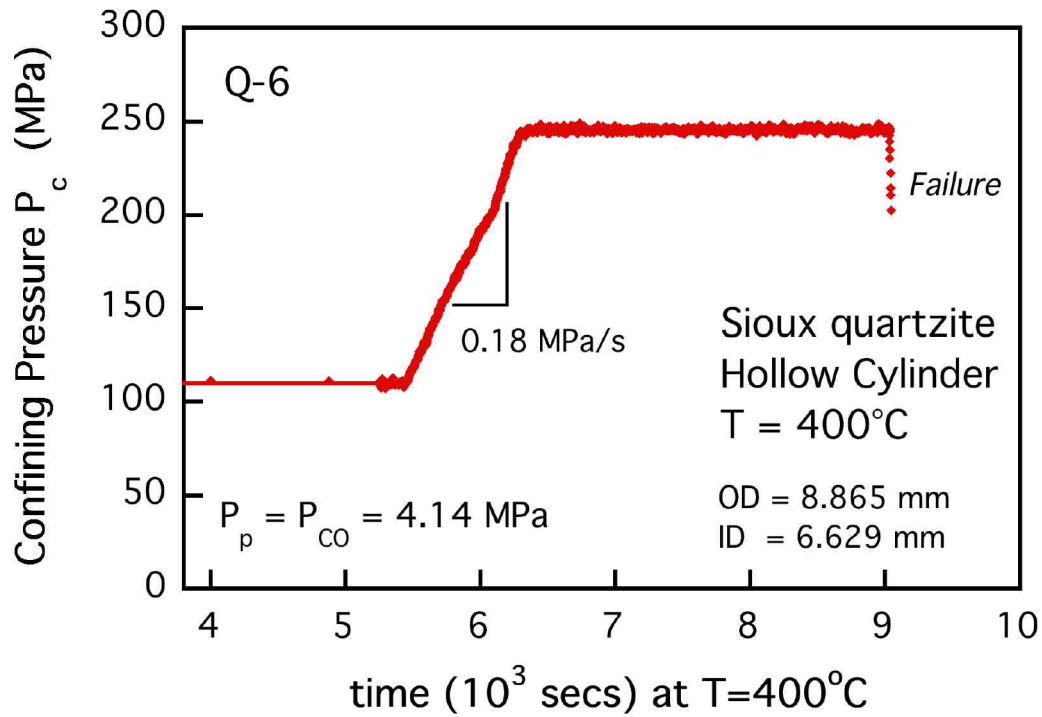
Figure 3. Confining pressure P_c versus time for experiment Q6. The sample was initially

pressurized to ~100 MPa, temperature increased to $T = 400°C$, and CO introduced as the

pore fluid. P_c was increased at 0.18 MPa/s until $P_c = 245.5$ MPa at which point it was

held constant. This sample failed at 2.7×10^3 s after the maximum P_c was reached, as

shown by the sudden drop in confining pressure due to a rapid argon leak through the

torn silver jacket. Time is shown in seconds after the experimental temperature was

reached.

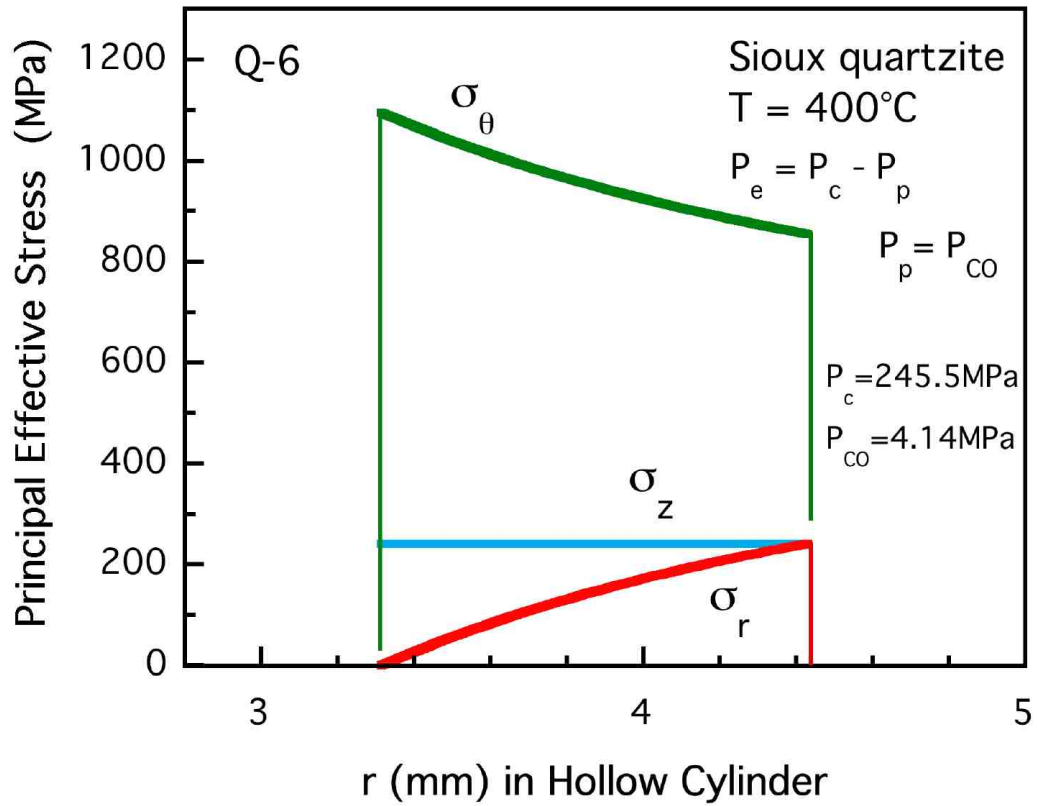721

722

723

724

725

726

727

728

729

729
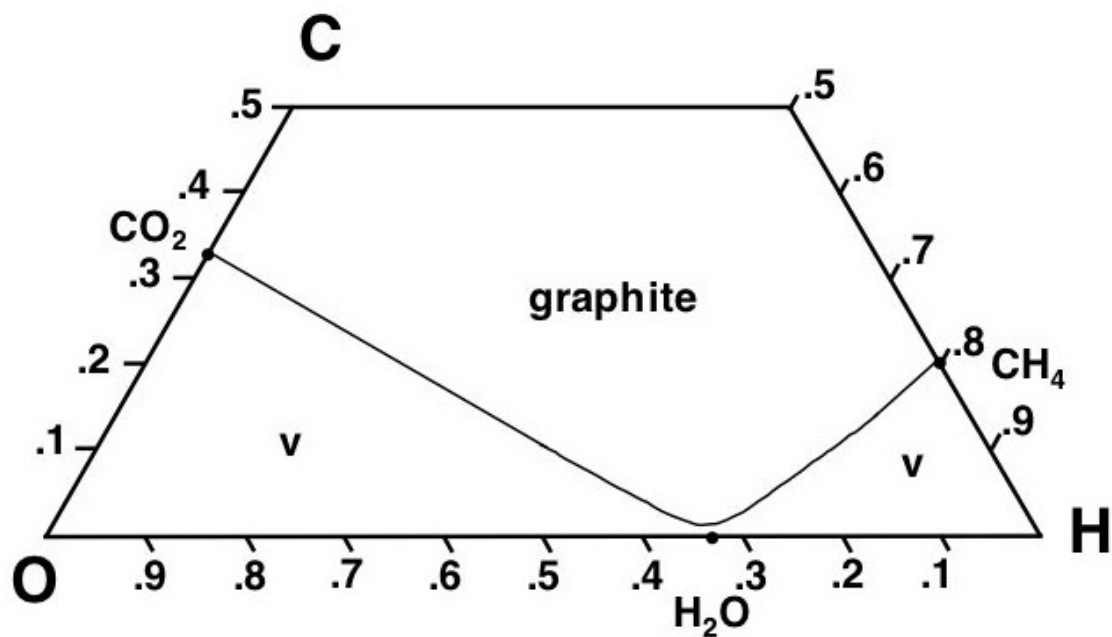
730

731 Figure 4. Compositions (atomic proportions) of graphite-saturated C-O-H vapor (V) at

732 400°C, 300 MPa [e.g., *Holloway,* 1984]. It can be seen that all mixtures of CO_2 and CH_4

733 are in the graphite field of stability.
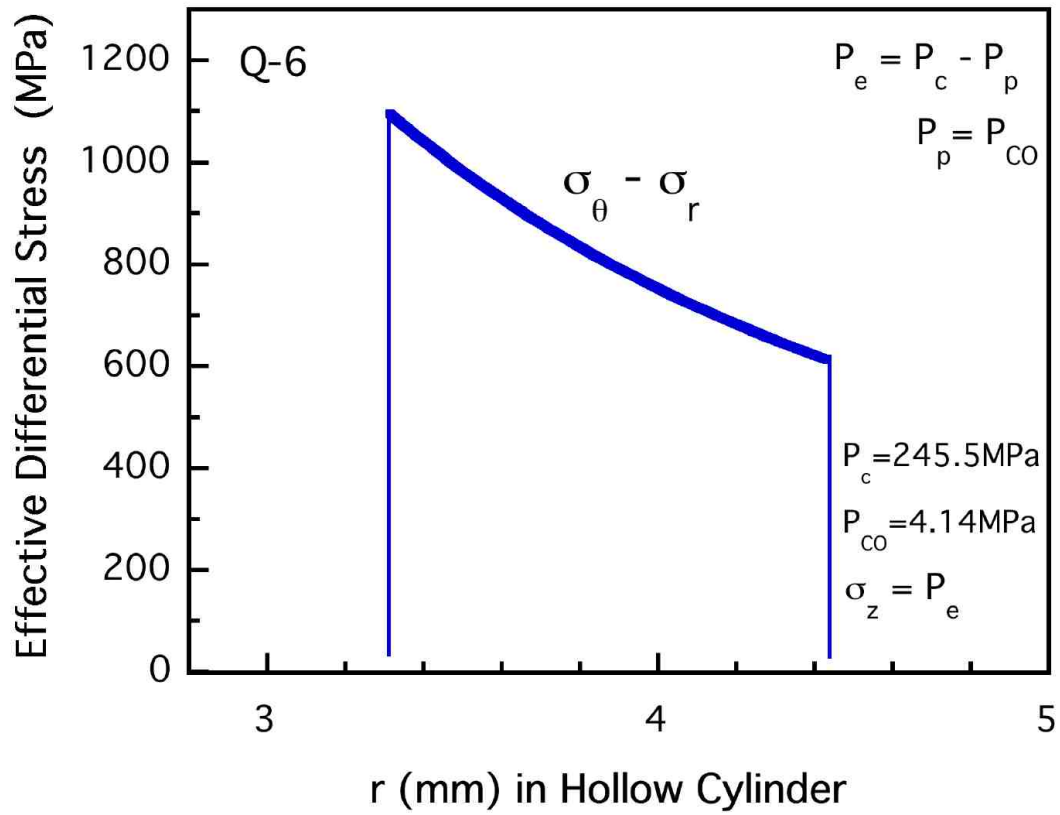
734

734

735

736   Figure 5. Principal effective stresses in hollow cylindrical sample of Sioux quartzite

737   (experiment Q6) as a function of radius r at the maximum confining pressure P_c applied,

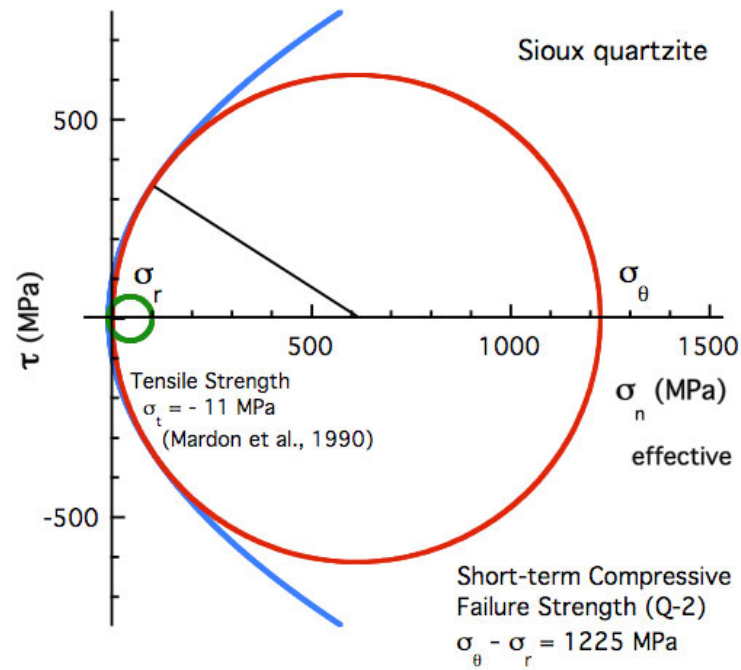738   based on the elastic solution of *Timoshenko and Goodier* [1970].

739

739

740

741 Figure 6. Effective differential stress (σ_q - σ_r) in hollow cylindrical sample of Sioux

742 quartzite (experiment Q6) as a function of radius *r* at the maximum confining pressure P_c

743 applied, based on the elastic solution of *Timoshenko and Goodier* [1970].

744

744

Sioux quartzite

τ (MPa)

500

σ_r

σ_θ

500 1000 1500

Tensile Strength
σ_t = - 11 MPa
(Mardon et al., 1990)

σ_n (MPa)

effective

-500

Short-term Compressive
Failure Strength (Q-2)
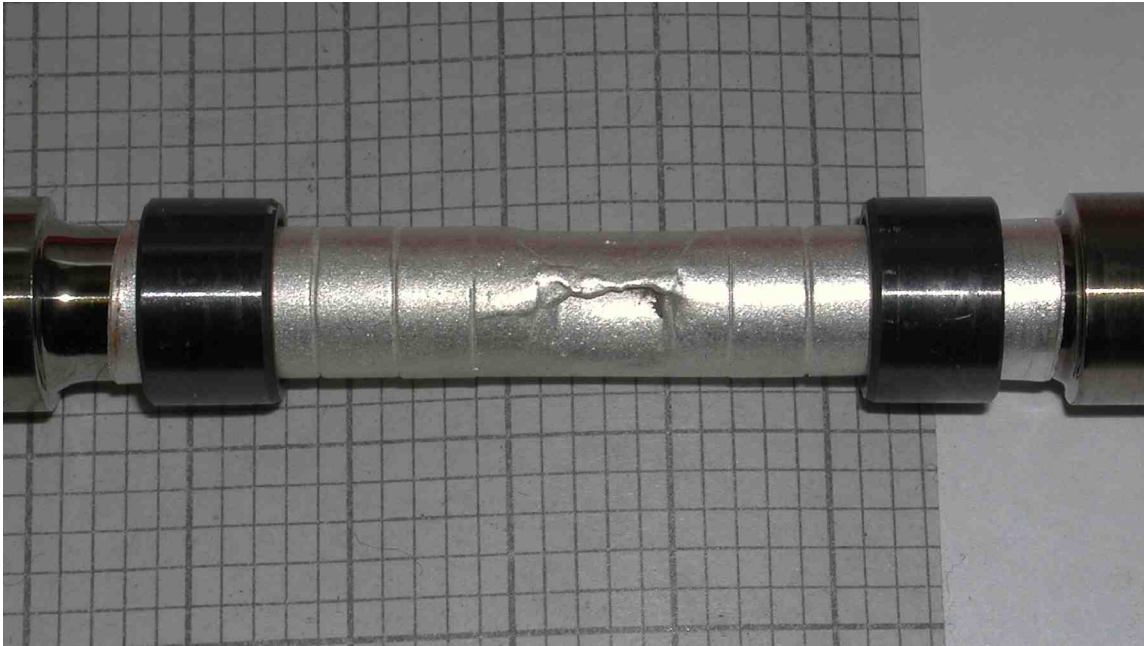σ_θ - σ_r = 1225 MPa

745

746   Figure 7. Mohr circle plot of Sioux quartzite compressive failure strength (maximum

747   effective differential stress, red for experiment Q2) compared with tensile strength

748   (green) reported by *Mardon et al.* [1990] for the same material at room temperature and *T*

749   = 412°C.

750

750

751

Figure 8. Hollow cylindrical Sioux quartzite in its piston-jacket assembly, immediately

after failure during experiment Q8. Failure of the sample is evident from the ruptured

silver jacket, with macroscopic shear Mode II fractures that are parallel to the cylinder

axis and transect the hollow cylinder wall. (Bold and minor chart paper divisions are

spaced 10 and 2 mm, respectively.)

757
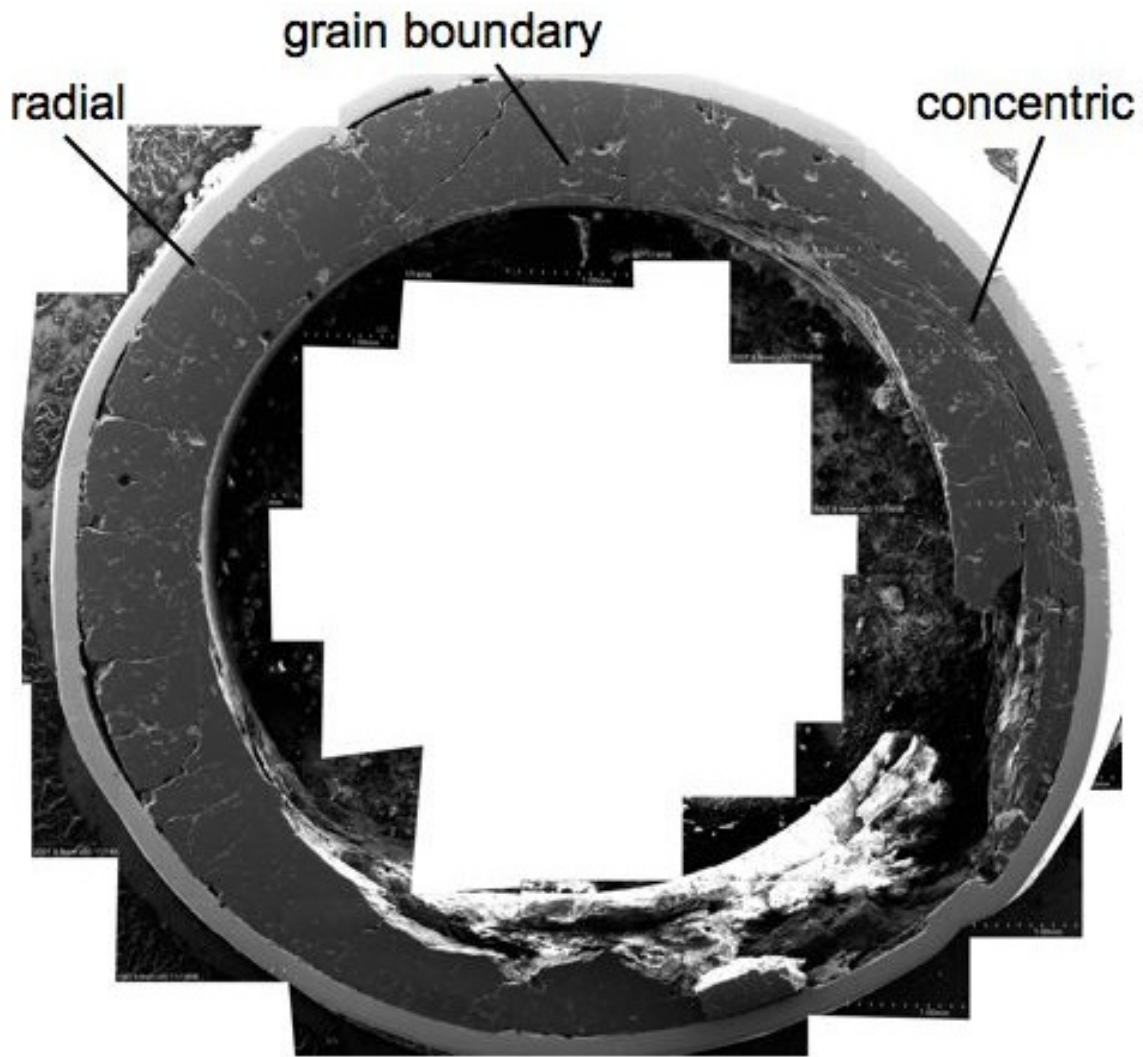
759   Figure 9. Mosaic of SEM images of cut and polished surface perpendicular to hollow

760   cylinder axis (Sioux quartzite sample Q6, coated with Au-Pd). Microcracks include grain

761   boundary cracks, concentric tensile Mode I cracks, concentric *en echelon* arrays of Mode

762   II cracks, macroscopic shear Mode II fractures that transect the cylinder wall, and radial

763   Mode I cracks.

764
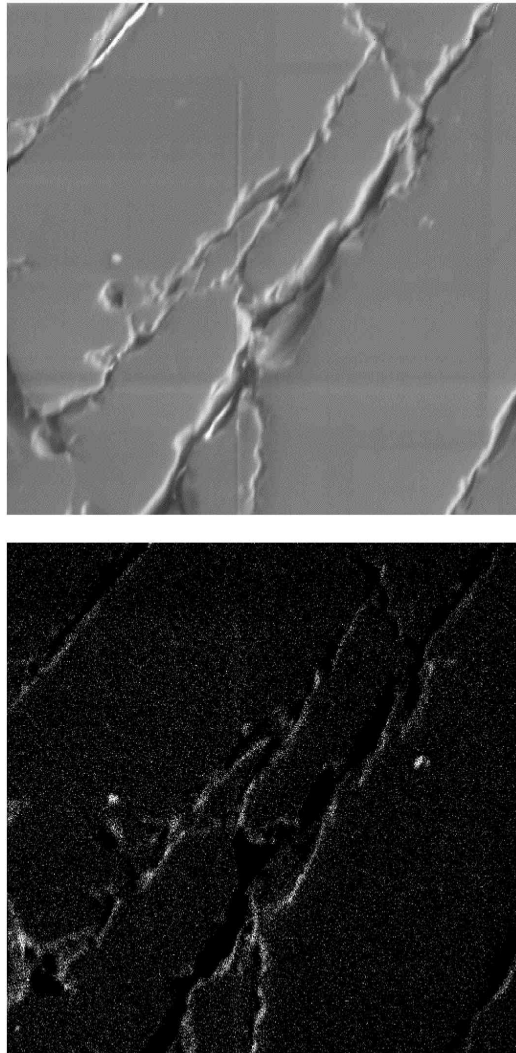
765

766 Figure 10. Polished surface perpendicular to axis of hollow cylindrical sample of Sioux

767 quartzite deformed at 400°C with CO pore fluid (Q6) showing microcracks formed

768 during the experiment, as observed by (a) secondary electron and (b) carbon x-ray

769 intensity map. In the latter, spot density is proportional to concentration. It can be seen

770 that the carbon films are well developed on the microcracks and fractures. The images

771 are 150 μm on a side.

772
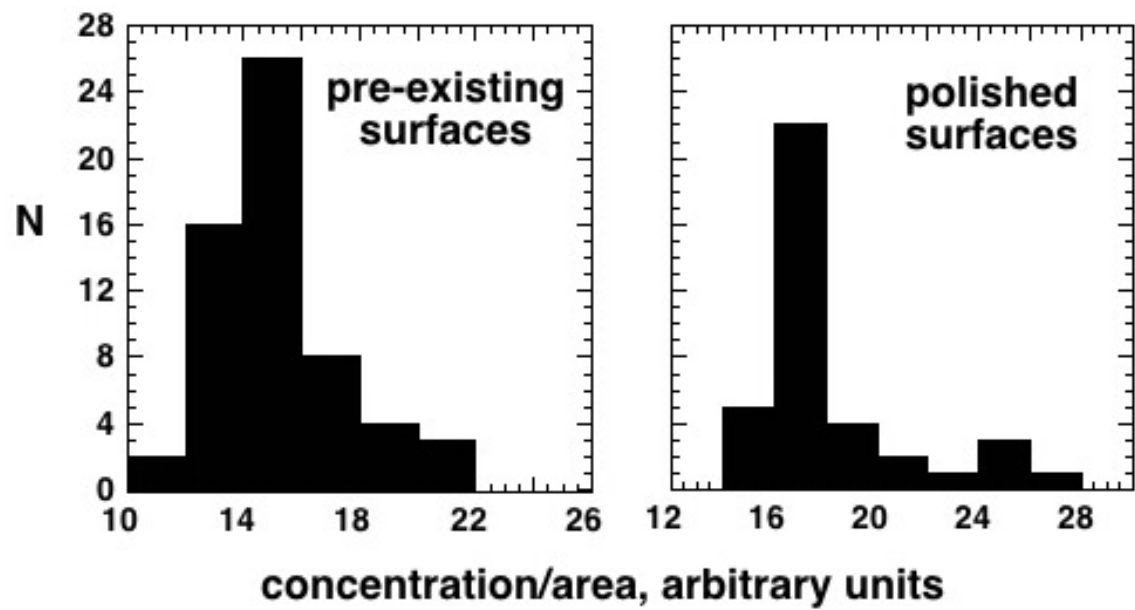
774   Figure 11. Histograms comparing carbon concentration normalized by area for (a) pre-

775   existing surfaces of sand grains (from samples Q4, Q7, Q9, Q10, Q11, Q12), and (b)

776   polished surfaces of Sioux quartzite.

777

777
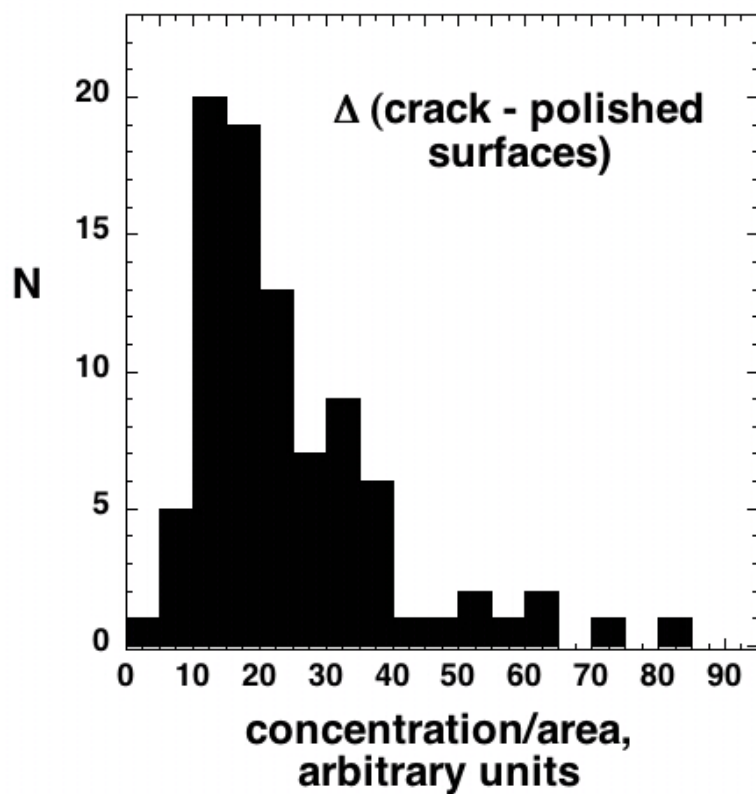
778

779 Figure 12. Histogram showing the difference between carbon concentration normalized

780 by area on crack surfaces and polished surfaces of Sioux quartzite (samples Q2, Q4, Q5,

781 Q6, Q9, Q10, Q11, Q12).

782

Table 1. Sioux quartzite hollow cylinder compression experiments.

Experi-ment	T (^{o}C)	Pore fluid	Pore pressure (MPa)	Pc rate (MPa/s)	Pc Max (MPa)	Pc resolu-tion (MPa)	Time at Pc Max (s)	Time at T (s)	Differen-tial stress (MPa)	Stress resolution (MPa)	Sample Failed?
Q1	25	CO	4.14	0.14	178.6	2.4	280	2.85×10^3*	730.2	10	N
Q2	400	CO	4.14	0.16	280.7	2.5	242	6.88×10^3	1225	11.1	Y
Q3	400	air	0.00	0.10	288.3	3.5	225	5.84×10^3	1201	14.6	Y
Q4	400	CO	4.14	0.12	250.0	3.1	2.53×10^4	9.76×10^4	1037	13.2	N
Q5	400	CO	4.14	0.18	247.0	2	110	5.54×10^3	1089	8.9	Y
Q6	400	CO	4.14	0.18	245.5	2.5	2.73×10^3	9.03×10^3	1095	11.6	Y
Q7	400	CO	4.14	0.17	203.7	2.5	1.37×10^4	2.44×10^4	904.6	11.1	N
Q8	400	CO	4.14	0.20	234.7	2.9	443	4.62×10^3	1051	13.5	N
Q9	400	CO	4.14	0.09	248.7	2.7	1.40×10^4	2.17×10^4	1071	11.9	N
Q10	400	CO2	1.97	0.10	257.4	1.6	209	5.19×10^3	1083	7.1	Y
Q11	400	CO2	4.14	0.09	237.4	2.8	246	2.81×10^3	1057	12.2	Y
Q12	400	50:50CO2 /CH4	4.17	0.10	229.4	3.7	210	7.33×10^3	1015	16.5	Y
Q13	400	50:50CO2 /CH4	4.23	0.11	222.3	2.8	1.44×10^4	1.78×10^4	931.2	12.1	N

Table 2. Results of electrical conductivity measurements on post-run samples.

Experiment	T (^{o}C)	Pore fluid	Pore pressure (MPa)	Geometric Shape Factor (m)	Max resistivity for geometry (MΩ-m)	Resistivity (MΩ-m)	Conductivity (S/m * 10^9)	Minimum Conductivity Enhancement	Sample Failed?
Q0	25	Air	4.14	0.226	22.6	OR	OR	--	N
Q6	400	CO	4.14	0.131	13.1	3.1	325	4.2	Y
Q7	400	CO	4.14	0.154	15.4	OR	OR	--	N
Q9	400	CO	4.14	0.151	15.1	2.9	349	5.2	N
Q12	400	50:50CO2 /CH4	4.17	0.266	26.6	16.5	61	1.6	Y
Q13	400	50:50CO2 /CH4	4.23	0.303	30.3	15.2	66	2.0	N

OR- Out of range of instrument (> 100 MΩ) 1.